2D Unsteady Navier-Stokes Computations at ONERA for Prediction of Dynamic Stall

O. Rouzaud
Research Scientist
ONERA, Châtillon
FRANCE

A. Plop *
Research Scientist
ONERA, Châtillon
FRANCE

This article presents the work in progress at ONERA for the numerical prediction of dynamic stall solving the Reynolds-averaged Navier-Stokes equations. Two numerical methods are under development.

The first one is based on a Jameson-type scheme with a fourth-stage Runge-Kutta time stepping integration and makes use of the implicit residual smoothing technique. To assess the method, the effect of the time step and the effect of the grid on the numerical predictions, several computations have been performed for a deep stall test case using either the Baldwin-Lomax turbulence model or the $k - \varepsilon$ Launder-Sharma turbulence model.

The second method stands on the dual-time stepping technique. Preliminary results are presented for two test cases of validation – an unsteady channel flow and an airfoil oscillating in pitch – providing a comparison of the efficiency of the two numerical methods.

NOTATIONS

c	:	speed of sound
C	:	airfoil chord
C_p	:	specific heat at constant pressure
E	:	total energy per unit volume
f	:	frequency
H	:	total enthalpy
Id	:	identity tensor
k	:	reduced frequency
k	:	turbulence kinetic energy
M	:	Mach number
n	:	outward normal to the surface
p	:	static pressure
P_r	:	Prandtl number
r	:	vector of the position
R_e	:	Reynolds number
s	:	grid velocity
S	:	surface element
t	:	time
T	:	static temperature
T	:	vector of the source term
V	:	vector of the absolute velocity
$\mathcal{V}$	:	volume element
W	:	vector of the absolute conservative unknowns
α	:	incidence angle
ε	:	turbulence energy dissipation

μ	:	dynamic viscosity
ρ	:	density
τ	:	dual time
$\pmb{\tau}$	:	stress tensor
ϕ	:	heat flux vector
ω	:	pulsation of the oscillating motion
Ω	:	vector of the angular velocity

Subscripts

e	:	inviscid value
i	:	stagnation value
t	:	turbulent value
v	:	viscous value
∞	:	upstream value

Mathematical notations

$\wedge$	:	vector product
$\otimes$	:	tensor product

INTRODUCTION

Dynamic stall appears on the retreating blade of a rotor and may lead to a massive separation on the upper surface of the blade. Although this phenomenon has been known for a long time, it is always a major

* National service during the year 97-98

challenge for helicopter design since, for instance, moment stall can greatly affect the flight performance of a helicopter and reduce the flight enveloppe. As a matter of fact, a lot of experimental and numerical work has been devoted to this problem.

Since the work of Mehta [1], many computations of the 2D unsteady Reynolds-averaged Navier-Stokes equations have been performed. According to these numerous works ([2]-[18]), the numerical prediction of dynamic stall raises many questions.

The first one is the turbulence modelling. The Baldwin-Lomax [19] algebraic turbulence model has been extensively used over the years because of its simplicity and also, in order to test the numerical methods. However, it is well-known that this model cannot give a correct description of the massive separation occuring on the upper surface. Computations involving one- and two-equations turbulence models have also been done [3, 5, 6, 10, 12, 14, 16, 17, 18]. As expected, a more complex turbulence model may improve the computation of the dynamic stall but the quantitative prediction of the phenomenon still seems out of reach. Tightly linked to the turbulence problem is the transition prediction. Although the influence of the transition of the boundary layer may be dramatic, most of the Navier-Stokes computations deal with a fully turbulent flow. Only Ekaterinaris $et.al.$ [12, 16] have proposed a transition criteria which is based on experimental knowledge of the dynamic stall. The transition onset is immediately downstream of the pressure peak on the upper surface. Their results clearly demonstrate the influence of transition on the numerical prediction of dynamic stall.

The last question is relative to the numerical method. Due to the unsteadiness of the flow and to the low reduced frequency involved, the need for an efficient method seems clear. The requirement for an implicit method is quite strong because, with an explicit method, the choice of the time step may be restricted by stability considerations rather than by time accuracy. A first possibility consists in using a factored/unfactored scheme with or without Newton subiterations. These subiterations remove the linearisation or the factorisation errors. Another choice is based on the dual-time stepping method [20] allowing the use of multigrid technique, local time stepping and implicit residual smoothing – techniques which are fully operational for steady-state consitions – along with a second-order time discretisation.

The aim of the paper is to present the two numerical methods developed at ONERA in the CANARI code for predictions of dynamic stall. The first method – which we will call Basic Numerical Scheme – corresponds to a Jameson scheme with a 4th-stage Runge-Kutta time-stepping integration using a cell-centred finite-volume discretisation. The Baldwin-Lomax model and the $k - \varepsilon$ Launder-Sharma model are retained for the turbulent simulations. In particular, the algebraic model has allowed to test the numerical method and to study the influence of the grid and of the time step on the numerical predictions. All the results have been obtained on a deep stall test case for the NACA0012 airfoil [21].

The other method is the dual-time stepping method. For the validation stage of this latter method, two test cases have been retained. The first test case corresponds to an unsteady channel flow and the numerical simulation is a Navier-Stokes computation using the algebraic model of Michel $et\ al.$ [22]. In this case, the grid is motionless. The second test case concerns a NACA0012 airfoil oscillating in pitch around its quarter chord [23]. The flow is transonic and Euler computations have been performed because the viscous effects are negligible. However, the grid has a rigid-body motion. Dynamic stall predictions using the dual-time stepping method are currently in progress.

GOVERNING EQUATIONS

The governing equations are the 2D Reynolds-averaged Navier-Stokes equations, written in a cartesian frame of reference which is attached to the body. In this non-inertial frame, the integral form of the conservation laws is

$$\frac{d}{dt}\left(\int_V \mathbf{W}\,d\mathcal{V}\right) + \int_S \mathbf{F}\cdot\mathbf{n}\,d\mathcal{S} = \int_V \mathbf{T}\,d\mathcal{V}$$

with

$$\mathbf{W} = \begin{pmatrix} \rho \\ \rho\mathbf{V} \\ \rho\mathbf{E} \end{pmatrix} \quad \mathbf{T} = \begin{pmatrix} 0 \\ -\rho\,\Omega\wedge\mathbf{V} \\ 0 \end{pmatrix}$$

$$\mathbf{F} = \begin{pmatrix} \rho\,(\mathbf{V} - \mathbf{s}) \\ \rho\mathbf{V}\otimes(\mathbf{V} - \mathbf{s}) + p\mathbf{Id} - \tau \\ \rho\mathbf{E}\,(\mathbf{V} - \mathbf{s}) + p\mathbf{V} - \tau\cdot\mathbf{V} + \phi \end{pmatrix}$$

The $\mathbf{W}$ term represents the vector $[\rho, \rho\mathbf{V}, \rho\mathbf{E}]^T$ of the conservative variables where the vector $\mathbf{V}$ is the absolute velocity vector, the components of which are written in the non-inertial frame. Due to the formulation, the time dependency of the airfoil frame leads to the presence of a source term $\mathbf{T}$ which appears in the right hand side of the momentum equations. Such a choice for the formulation is in agreement with previous computational works [24, 25] since it ensures an accurate treatment of the convective fluxes and of the boundary conditions in the farfield.

The pressure p is obtained through the equation of state for a perfect gas

$$p = (\gamma - 1)\left(\rho E - \rho\frac{V^2}{2}\right)$$

The stress tensor τ and the heat flux vector ϕ are represented by viscous and turbulent components

$$\begin{aligned}\tau &= \tau_v + \tau_t\\\phi &= \phi_v + \phi_t\end{aligned}$$

For a Newtonian fluid using the Stokes hypothesis, the expression of the viscous stress tensor τ_v is

$$\tau_v = \mu\left(\nabla V + \nabla V^T - \frac{2}{3}\left(\nabla\cdot V\right)\mathrm{Id}\right)$$

where μ is the dynamic viscosity obtained with the Sutherland law. Through the Boussinesq's hypothesis, the expression of the Reynolds or turbulent stress tensor τ_t is

$$\tau_t = \mu_t\left(\nabla V + \nabla V^T - \frac{2}{3}\left(\nabla\cdot V\right)\mathrm{Id}\right) - \frac{2}{3}\rho k\mathrm{Id}$$

and μ_t is the turbulent viscosity given by the chosen turbulence model.
Both components of the heat flux vector obey Fourier's law of heat conduction

$$\begin{aligned}\phi_v &= \frac{\mu\,C_p}{P_r}\nabla T\\\phi_t &= \frac{\mu_t\,C_p}{P_{rt}}\nabla T\end{aligned}$$

where P_r and P_{rt} are respectively the Prandtl number and the turbulent Prandtl number.

The vector s is the velocity vector of the grid and Ω is the vector of rotation of the non-inertial frame relatively to the absolute one. The grid being non-deforming with a rigid-body motion, the velocity of a mesh point is

$$s = \Omega\wedge(r - r_0)$$

where r and r_0 stand respectively for the vector position of the point and the vector position of the rotational axis.

Finally, the turbulent viscosity is estimated either with the Baldwin-Lomax algebraic turbulence model [19] or with the $k - \epsilon$ Launder-Sharma two equations model [26]. In this last case, the convective terms of the transport equations are modified due to the rigid-body motion. The differential form of these

equations is thus

$$\frac{\partial(\rho k)}{\partial t} + \nabla\cdot(\rho k\left(V - s\right)) = \tau_t\nabla V - \rho\varepsilon - 2\mu\nabla k.\nabla k$$
$$+\ \nabla\cdot\left(\left(\mu + \frac{\mu_t}{\sigma_k}\right)\nabla k\right)$$

$$\frac{\partial(\rho\epsilon)}{\partial t} + \nabla\cdot(\rho\varepsilon\left(V - s\right)) = C_{\varepsilon 1}\frac{\varepsilon}{k}\tau_t\nabla V - \rho C_{\epsilon 2}f_2\frac{\varepsilon^2}{k}$$
$$+\ \nabla\cdot\left(\left(\mu + \frac{\mu_t}{\sigma_\varepsilon}\right)\nabla\varepsilon\right)$$
$$+\ 2\frac{\mu\,\mu_t}{\rho}\nabla\left(\nabla V\right).\nabla\left(\nabla V\right)$$

with

$$\begin{aligned}f_2 &= 1 - 0.3exp\left(-R_t^2\right)\quad;\quad R_t = \frac{k^2}{\nu\varepsilon}\\C_\mu &= 0.09\,;\,C_{\varepsilon 1} = 1.44\,;\,C_{\varepsilon 2} = 1.92\\\sigma_k &= 1\,;\,\sigma_\varepsilon = 1.3\end{aligned}$$

The term R_t defines the turbulent Reynolds number and the turbulent viscosity is given by

$$\mu_t = \rho C_\mu f_\mu\frac{k^2}{\varepsilon}\quad;\quad f_\mu = exp\left(\frac{-3.4}{(1 + R_t/50)^2}\right)$$

NUMERICAL METHOD

Basic Numerical Scheme (BNS)

The CANARI code [27, 28] is a multidomain solver for structured meshes with a cell-centred finite-volume discretisation. The numerical scheme corresponds to the Jameson scheme [29] following the method of lines by decoupling the approximation of the spatial and temporal discretisations. For a model problem, the equations are written

$$\frac{\partial W}{\partial t} + C(W) = 0$$

where $C(W)$ represents the convective and diffusive fluxes. The steady-state implementation contains convergence acceleration techniques such as local time stepping, FAS multigrid method [30] using V-cycles and the implicit residual smoothing of Lerat et al. [31]. For turbulent computations, several turbulence models are available including the Baldwin-Lomax model and the $k - \varepsilon$ model of Launder-Sharma [32].

Concerning the explicit stage, second-order central differences are used for all spatial derivatives. A blend of linear 4th-difference-based and 2nd-difference-based artificial dissipation $D(W)$ is added in scalar form to suppress the odd-even decoupling and to prevent the appearance of oscillations in the neighborhood of shock waves or stagnation points

$$\frac{\partial W}{\partial t} + C(W) - D(W) = 0$$

The solution is then advanced explicitly in time with a 4th-stage Runge-Kutta time-stepping algorithm. If n is the index associated with time and by denoting $R(W) = C(W) - D(W)$ as the residual term, the algorithm is written as

$$W^{(0)} = W^n$$
$$W^{(1)} = W^{(0)} - \alpha_1 \Delta t\, R^{(0)}(W)$$
$$W^{(2)} = W^{(0)} - \alpha_2 \Delta t\, R^{(1)}(W)$$
$$W^{(3)} = W^{(0)} - \alpha_3 \Delta t\, R^{(2)}(W)$$
$$W^{(4)} = W^{(0)} - \alpha_4 \Delta t\, R^{(3)}(W)$$
$$W^{n+1} = W^{(4)}$$

where the values of the α_k coefficients are $1/4$, $1/3$, $1/2$, 1. The choice of the last coefficient ensures the consistency while the last two values provide a second-order time discretisation if the flux terms of the last stage are computed with the values W of the third stage.

The implicit stage corresponds to the implicit residual smoothing technique of Lerat et al. [31], originally developed for the Euler equations. It has been extended to the Navier-Stokes equations. In this case, the implicit method preserves the time accuracy of the explicit stage and ensures an unconditional stability [33, 34]. Modifications of the implicit method, to take into account the Jacobian of the viscous terms, are possible but reduce the time discretisation to order one. The numerical boundary conditions for the implicit conditions are Neumann type boundary conditions. In the paper, the turbulent computations of dynamic stall are first-order accurate in time since the viscous terms are frozen at the first stage of the Runge-Kutta scheme in order to save up computational time. Note also that the same choice stands for the dissipative terms.

The present computations require the treatment of three types of boundaries. At the wall, the relative velocity $(V - s)$ is zero because of the no-slip condition and the airfoil surface is also adiabatic. For the farfield boundaries, non-reflecting boundary conditions are applied. Lastly, at the wake cut, continuity of the conservative variables is ensured.

Dual-Time Stepping Method (DTS)

The DTS method aims at the resolution of unsteady equations with a time-marching steady-state solver using the usual acceleration techniques such as local time stepping, multigrid, implicit residual smoothing while providing a second-order time accuracy. In order to do so, the governing equations have to be reformulated with the introduction of a dual time τ.

To illustrate this point, consider the unsteady model equation

$$\frac{\partial W}{\partial t} + R(W) = 0$$

where $R(W)$ is the residual term which contains the convective, diffusive and artificial dissipation fluxes. The introduction of a dual time derivative of the conservative variables leads to

$$\frac{\partial W}{\partial \tau} + \frac{\partial W}{\partial t} + R(W) = \frac{\partial W}{\partial \tau} + R^*(W) = 0$$

The term $R^*(W)$ corresponds to the unsteady residual. Performing subiterations in the dual time τ allows to use a time-marching steady-state solver and, at convergence $(R^*(W) = 0)$, to obtain the solution of the unsteady equation.

In the unsteady residual, the discretization of the flux term is similar to the discretization of the basic numerical method. On the other hand, a three-point backward formula gives the time derivative $\frac{\partial W}{\partial t}$ and results in a time implicit scheme which is second-order accurate in time

$$\frac{\partial W}{\partial \tau} + \frac{3W^{n+1} - 4W^n + W^{n-1}}{2\Delta t} + R(W^{n+1}) = 0$$

Note that the indices are relative to the physical time. Due to the use of two different times, the stability analysis of the method requires the treatment of two problems. The first one concerns the stability of the physical problem [20]

$$\frac{3W^{n+1} - 4W^n + W^{n-1}}{2\Delta t} + R(W^{n+1}) = 0$$

which does not set any trouble because the second-order backward difference scheme is A-stable. The second analysis lies on the stability analysis of the dual time solver. According to a linear analysis of the Runge-Kutta scheme applied to the model equation, the dual time step $\Delta \tau$ in each cell is expressed as

$$\Delta \tau = \text{Min}\left(\Delta \tau_e , \Delta \tau_v , \frac{2\Delta t}{3} \right)$$

with

$$\Delta \tau_e = CFL \frac{L}{V + c}$$
$$\Delta \tau_v = CFL \frac{\rho L^2}{2\gamma \left(\frac{\mu}{Pr} + \frac{\mu_t}{Pr_t} \right)}$$

where L is a characteristic length of the mesh cell and c is the local speed of sound. The two time steps $\Delta \tau_e$ and $\Delta \tau_v$ respectively take into account the convection and diffusion limitations.

In order to manage the number of subiterations in dual

time, between the physical times t and $t + \Delta t$, it is possible to specify the number of subiterations or to define a tolerance criterion. In the ONERA method, the second choice has been retained and the tolerance criterion is satisfied once the root mean square of the first component of the residual $R^*(W)$ is less than a prescribed value. The checking of the tolerance criterion is equivalent to the end of one time step in physical time.

Once the tolerance criterion is reached, it is necessary to update the time derivative $\frac{\partial W}{\partial t}$ and to provide an initial solution for the next time step. A three-point backward linear interpolation gives the new solution

$$W = W^n + \frac{3W^n - 4W^{n-1} + W^{n-2}}{2}$$

Note that, at the beginning of an unsteady computation, a first-order time discretisation replaces the second-order relation.

Grid Generation

The grid generation is performed with an hyperbolic grid generator [35] enabling to get C-topology or 0-topology around an airfoil. Such a grid generator ensures the regularity and the orthogonality of the mesh although the location of the farfield boundaries is not perfectly managed. These two properties of regularity and orthogonality are very important in order to give a good description of the boundary layer.

RESULTS WITH THE BNS

All the computations presented in the article have been performed on a Fujitsu VX2 computer. The steady state solution at the mean angle of incidence provides the initial solution for the unsteady computation. The periodic regime of the unsteady solution is said to be reached when the evolution of the global coefficients from one cycle to the other is similar. It usually takes three periods to reach the periodic regime. The computational cost of one time step per cell and per point for the basic numerical method costs approximately $7\mu s$ for the Baldwin-Lomax computations and $10\mu s$ for the Launder-Sharma computations.

Three grids have been built for the computations. They all have a C-topology and their respective dimensions are 257x65, 321x97 and 385x97. At the wall, the height of the first cell is worth to $0.00001C$ which corresponds to a dimensionless height y^+ of order unity. The radial extension of the grids is close to $20C$. The figures 1 and 2 present views of the coarse grid around the NACA0012 airfoil, the second one demonstrating the regularity of the mesh.

Description of the Test Case

The test case comes from the experimental work of McAlister et al. [21]. It corresponds to the referenced frame 14106 with the following test conditions

$$\begin{aligned}
M_\infty &= 0.184 & \text{Re} = \frac{\rho_\infty V_\infty C}{\mu_\infty} = 2.45\text{x}10^6 \\
\alpha(t) &= 10^o + 15^o \sin(\omega t) \\
k &= \frac{\omega C}{2V_\infty} = 0.0994
\end{aligned}$$

The airfoil is oscillated in pitch around its quarter chord axis. In this test case, a boundary-layer trip is located at the leading edge in order to eliminate the laminar separation bubble. The flow can thus be regarded as fully turbulent. Note that this test case corresponds to a deep stall case.

Effect of the grid

In order to test the influence of the grid on the numerical solutions, computations have been performed on the three grids using the same dimensionless time step $\Delta t = 0.0001$ (reference time $C/a_{i\infty}$). A whole cycle is covered in 172000 time steps. The order of magnitude of the maximal CFL number is around 125. Figure 3 shows the comparison between the numerical results and the experimental data for the lift, the moment and the drag coefficients.

At first, we notice that the numerical results are qualitatively correct but important discrepancies with the experimental data are obvious. For instance, all the predictions delay the occurence of the moment stall or of the lift stall. Furthermore, oscillations of the global coefficients appear during the downstroke part of the motion. Although the experimental values are averaged over several cycles, these oscillations seem of a numerical origin.

Concerning the influence of the grid, a grid convergence seems to be reached between the medium and the fine grid. Due to this fact, all the other Baldwin-Lomax computations have been performed on the fine grid. The coarse grid results are significantly different but provide the best estimations of the moment stall, the lift stall and the drag increase.

Effect of the time step

Figure 4 illustrates the effect of the time step on the numerical predictions of the global coefficients on the finer grid. The dimensionless time steps are equal to 0.0005, 0.001 and 0.002. The time step effects are not very important, the main discrepancies appearing during the downstroke motion between the solution $\Delta t = 0.002$ and the two other computations. By the way, it demonstrates the time convergence of the calculations and the reliability of the basic numerical method.

Grid 385x97

This paragraph presents a more physical description of the dynamic stall prediction on the finest grid using the time step $\Delta t = 0.0001$. Emphasis is laid on the first half of the oscillating motion (from $15°$ up to $15°$ down) and especially to the formation and convection of the first stall vortex.

Figure 5 gives the evolution of the predicted global coefficients during the third computed period versus the phase angle $\phi = \omega t$. Starting from the mean angle of incidence in the upstroke motion, the coefficients obey a quasi-steady behaviour till the angle of $60°$ where the moment stall begins. The moment coefficient decreases suddenly attaining a first peak at $90°$, increases and decreases again to reach a second peak around $105°$. New oscillations occur around $135°$ and $180°$ before the reattachment of the flow at the end of the downstroke motion. The lift coefficient and the drag coefficient experiment the same kind of evolution but with a slight delay when compared with the moment behaviour. For instance, the lift stall or the drag decrease appear $30°$ later relatively to the moment stall. Figure 6 shows the distribution of the pressure coefficient on the airfoil surface, the phase angle varying from $10°$ to $180°$. For the first six locations, it is clear that the suction pressure peak increases with the angle of incidence. Between $60°$ and $70°$, there is a brutal breakdown of the pressure peak and the presence of the stall vortex is clear at $70°$ ($x/c = 0.1$). The convection of the vortex takes place up to a phase angle close to $90°$. As mentioned previously, new events occur in the following positions, in particular at the trailing edge, due to the growth and convection of other vortices.

In the next figure 7, the pressure distribution is plotted for several chordwise locations versus the phase angle. In the upper plot, the phase angle describes the first half of the cycle while the bottom figure only contains the interval between $60°$ and $120°$. The dramatic breakdown of the peak pressure clearly appears in the upper figure near a phase angle of $60°$. Note also the perturbations of the pressure distribution during the oscillating motion. The lower plot provides an estimation of the convection speed of the first stall vortex because the pressure peak denotes the presence of a vortex. A crude approximation gives a convection speed close to $0.3\,V_\infty$ in accordance with usual experimental values.

The instantaneous streamlines are plotted on Figure 8 between the phase angles $50°$ and $190°$, every $10°$. The view confirms the previous explanations. The growth and convection of the first two stall vortices are clearly seen. Furthermore, small structures appear and vanish at the leading edge and at the trailing edge during the oscillating motion. Finally, note that the stall effects seem to disappear after a phase angle of $190°$.

Launder-Sharma Computations

Due to the computational cost, the computations have only been performed on the medium grid for a dimensionless time step $\Delta t = 0.0002$. It takes 862670 time steps to cover one period.

Figure 9 gives a comparison of the global coefficients between the experimental data and the numerical results due to the Baldwin-Lomax computation and the Launder-Sharma computation. The main conclusion is that the use of the Launder-Sharma turbulence mode does not improve the prediction of the dynamic stall. When compared to the Baldwin-Lomax results, the Launder-Sharma computation gives an earlier moment stall or an earlier drag increase. The global coefficients have also a less oscillatory behaviour during the downstroke motion. However, the lift estimate in the upstroke motion is even worse than for the Baldwin-Lomax computation. These results strongly underline the need to extend the numerical method to other transport equations turbulence models.

RESULTS WITH THE DTS

Channel Flow

The test case is based on a steady channel flow (Délery bump – case B [36]) for which the experimental conditions are

$$M_\infty = 1.45 \qquad \text{Re} = 2.078 \times 10^6$$

with a dimensionless downstream pressure fixed to 0.675. A quite simple unsteady test case – useful for numerical validation – consists in prescribing a sinusoidal law to the downstream pressure

$$p = p_s\left(1 + \alpha sin(\omega t)\right) \qquad p_s = 0.675$$

The dimensionless period is equal to 4. The computations have been performed on a H-topology grid (Fig.10) with 181 points along the streamwise direction and 65 in the normal direction using the BNS method and the DTS method. The algebraic turbulence model of Michel et al. [22] provides an estimate of the turbulent viscosity.

For the BNS method, the dimensionless time step is equal to $\Delta t = 0.001$ (4000 time steps per period) leading to a $CFL_{\max}$ number close to 20. The implicit residual smoothing technique is employed without its viscous part and the time discretisation is second-order accurate. The computational time for one period is equal to 334s on the Fujitsu VX2 computer. For the DTS computation, the time step is $\Delta t = 0.1$

(400 time steps per period). During the subiterations, the method makes use of the local time stepping ($CFL = 4$), of the implicit residual smoothing and of the multigrid technique including two grid levels with two iterations on the coarse grid. Due to the tolerance criterion, the computation requires approximately 15 subiterations per time step. Lastly, the computational time to cover one period is 85s.

Figure 11 shows a comparison of the time evolution of the pressure at several locations in the channel for both numerical methods. It takes two periods to get a periodical behaviour. In both computations, the pressure levels are quite close although the shape of the curves are slightly different. The next figure (Fig.12) presents the Mach number contours obtained with the DTS method during the fifth period. The plots show a shock/boundary layer interaction on the rear of the bump and a pressure wave moving periodically from downstream to the shock. The BNS method gives similar results.

AGARD CT1 Test Case

The test case comes from the experimental wotk data collected in the AGARD Report No.702 [23]. It has be chosen to test the DTS method with a non-deforming moving grid. The test configuration is

$$
\begin{aligned}
M_\infty &= 0.6 \quad Re = \frac{\rho_\infty V_\infty C}{\mu_\infty} = 4.8 \times 10^6 \\
\alpha(t) &= 2.89^\circ + 2.41^\circ \sin(\omega t) \\
k &= 0.0808
\end{aligned}
$$

The airfoil oscillates in pitch around the quarter-chord axis. The grid contains 257x65 nodes. The height of the first cell is $0.001C$ along the airfoil and the farfield extension is close to $8C$.

For the BNS method, the computations are first-order accurate in time. The CFL_{max} number is close to 65. The dimensionless time step is $\Delta t = 0.03$ and 2160 time steps are necessary to cover one period, corresponding to a computational time per period worth to 180s. For the DTS method, the time step is $\Delta t = 1.8$ and only 36 time steps are required for one cycle. The local CFL number is equal to 9. Two grid levels are used with the multigrid method with three iterations on the coarse grid. For the dual time convergence, an average of 33 subiterations is necessary to cover one time step. The CPU time is worth to 215s meaning that the BNS method is more efficient than the DTS one. No explanation has been found yet, but the BNS method seems quite efficient in this case because of a CFL number value. Further work is needed to fully explore the efficiency of the two methods.

In order to check the validity of the numerical results,

figure 13 presents a comparison of the lift and moment coefficients from the experimental data and the results provided by the two methods. It takes three periods to attain a periodical regime and the numerical predictions are very similar for both coefficients. Note that the discrepancies on the moment coefficient between the experimental data and the numerical results have been already reported (for instance, [37]). They seem to be due to a bad experimental location of the rotational axis.

CONCLUSIONS

From the present study, one can draw several conclusions about the two numerical methods and define future goals for the prediction of the dynamic stall phenomenon.

From a physical point of view, it is clear that, even if the use of the Baldwin-Lomax or the $k - \varepsilon$ Launder-Sharma turbulence models enabled to validate the BNS method, the numerical results are not very satisfactory for the prediction of dynamic stall. New computations have to be performed with other turbulence models following the work of Ko and Mc-Croskey [14], for instance.

From a numerical point of view, the BNS method seems quite efficient for unsteady Navier-Stokes simulations, at least when an algebraic turbulence model is used. However, its efficiency is not so clear with the Launder-Sharma turbulence model. Further work is needed to point out the possible limitations of the method for unsteady computations. Regarding the DTS method, the preliminary results are quite encouraging for the channel flow but the oscillating airfoil test case raises some questions. The comparison of the performances of the two numerical methods requires some new simulations. In particular, it is planned to perform stall computations with the DTS method and to extend the use of the method to simulations with transport-equations turbulence models [38, 17, 18].

Beyond these tasks, efforts will be put on the use of a high-order numerical scheme [39, 40] and an automatic grid adaption method [41] since such approaches could lead to a better prediction of the dynamic stall phenomenon.

References

[1] U.B. Mehta. *Dynamic Stall of an Oscillating Airfoil*. AGARD-CP227, Unsteady Aerodynamics,

Paper 23, 1977.

[2] J.A. Ekaterinaris. *Compressible Studies on Dynamic Stall*. AIAA Paper 89-0024, 27th Aerospace Sciences Meeting, Reno (NV), USA, 1989.

[3] J. Wu, L. Sankar and D. Huff. *Evaluation of Three Turbulence Models for the Prediction of Steady and Unsteady Airloads*. AIAA Paper 89-0609, 27th Aerospace Sciences Meeting, Reno (NV), USA, 1989.

[4] M.R. Visbal. *Dynamic Stall of a Constant-Rate Pitching Airfoil*. J. of Aircraft, Vol.27, No.5, 1990.

[5] J.D. Clarkson, J.A. Ekaterinaris and M.F. Platzer. *Computational Investigation of Airfoil Stall Flutter*. 6th Int. Symposium on Unsteady Aerodynamics, Aeroacoustics and Aeroelasticity, H.M. Atassi Ed., Springer-Verlag, 1991.

[6] M. Dindar and U. Kaynak. *Effect of Turbulence Modeling on Dynamic Stall of a NACA0012 Airfoil*. AIAA Paper 92-0027, 30th Aerospace Sciences Meeting and Exhibit, Reno (NV), USA, 1992.

[7] W. Geissler and H. Vollmers. *Unsteady Separated Flows on Rotor Airfoils*. Paper No.79, 18th European Rotorcraft Forum, France, 1992.

[8] T. Reu and S.X. Ying. *Hybrid Grid Approach to study Dynamic Stall*. AIAA J., Vol.30, No.11, 1992.

[9] D.P. Rizetta and M.R. Visbal. *Comparative Numerical Study of Two Turbulence Models for Airfoil Static Stall and Dynamic Stall*. AIAA J., Vol.31, No.4, 1993.

[10] G.R. Srinivasan, J.A. Ekaterinaris and W.J. McCroskey. *Dynamic Stall of an oscillating Wing. Part 1 : Evaluation of Turbulence Models*. AIAA Paper 93-3403, AIAA 11th Applied Aerodynamics Conference, Monterey (CA), USA, 1993.

[11] J.A. Ekaterinaris, A.S. Cricelli and M.F. Platzer. *A Zonal Method for Unsteady Viscous Compressible Airfoil Flows*. J. of Fluids and Structures, Vol.8, 1994.

[12] J.A. Ekaterinaris and F.R. Menter. *Computations of Separated and Unsteady Flows with One- and Two-Equation Turbulence Models*. AIAA J., Vol.32, No.12, 1994.

[13] C.Q. Lin and K. Pahlke. *Numerical Solution of Navier-Stokes Equations for Rigid Airfoils in Arbitrary Unsteady Motion*. DLR Report IB 129-94/20, 1994.

[14] S. Ko and W.J. McCroskey. *Computations of Unsteady Separating Flows over an Oscillating Airfoil*. AIAA Paper 95-0132, 33rd Aerospace Sciences Meeting and Exhibit, Reno (NV), USA, 1995.

[15] B.B. Prananta, M.H.L. Hounjet and R.J. Zwaan. *Thin-Layer Navier-Stokes Solver and its Application for Aeroelastic Analysis of an Airfoil in Transonic Flow*. Royal Aeronautical Soc., Forum on Aeroelasticity and Structural Dynamics, London, England, 1995.

[16] J.A. Ekaterinaris and M.F. Platzer. *Numerical Investigation of Stall Flutter*. J. of Turbomachinery, Vol.118, 1996.

[17] Y.-Y. Niu and M.-S. Liou. *Numerical Simulation of Dynamic Stall using Upwind Methods with Dual Time Stepping*. AIAA Paper 97-1000, 1997.

[18] Y.-Y. Niu. *Numerical Simulation of Dynamic Stall using Upwind Methods and RNG Turbulence Models*. AIAA Paper 98-0419, 36th Aerospace Sciences Meeting and Exhibit, Reno (NV), USA, 1998.

[19] B.S. Baldwin and H. Lomax. *Thin Layer Approximation and Algebraic Model for Separated Turbulent Flows*. AIAA Paper 78-0257, 1978.

[20] A. Jameson. *Time Dependent Calculations using Multigrid with Applications to Unsteady Flows past Airfoils and Wings*. AIAA Paper 91-1259, 10th Computational Fluid Dynamics Conference, Honolulu (HI), USA, 1991.

[21] K.W. McAlister, S.L. Pucci and W.J. McCroskey. *An experimental Study of Dynamic Stall on Advanced Airfoil Sections*. NASA Technical Memorandum 84245, 1982.

[22] R. Michel, C. Quémard and R. Durant. *Application d'un Schéma de Longueur de Mélange à l'Etude des Couches Limites Turbulentes d'Equilibre*. ONERA, Technical Note No.154, 1969.

[23] Collective work. *Compendium of Unsteady Aerodynamic Measurements*. AGARD Report No.702, 1982.

[24] R.K. Agarwall and J.E. Deese. *Euler Calculations for Flowfield of a Helicopter Rotor in Hover*. AIAA Paper 86-1782, 1986.

[25] J.-C. Boniface. *Calculs d'Ecoulements Compressibles autour de Rotors d'Hélicoptères en Vol Stationnaire ou en Vol d'Avancement par Résolution des Equations d'Euler.* PhD thesis, ENSAM, 1995.

[26] B.E. Launder and B.I. Sharma. *Application of Energy-Dissipation Model of Turbulence to the calculation of Flow near a Spinning Disc.* Letters in Heat and Mass transfer, Vol.1, 1974.

[27] A.-M. Vuillot, V. Couaillier and N. Liamis. *3-D Turbomachinery Euler and Navier-Stokes Calculations with a Multidomain Cell-Centered Approach.* AIAA/SAE/ASME/ASEE 29th Joint Propulsion Conference on Exhibit, Monterey (CA), USA, 1993.

[28] V. Couaillier. *Recent Developments performed at ONERA for the Simulation of 3D Inviscid and Viscous Flows in Turbomachinery by the Solution of Euler and Navier-Stokes Equations.* In Proceedings of the 9th ISABE Symposium, edited by F.S. Billig, Washington D.C., 1993.

[29] A. Jameson, W. Schmidt and E. Turkel. *Numerical Solution of the Euler Equations by Finite Volume Methods using Runge-Kutta Time Stepping Schemes.* AIAA Paper 81-1259, 14th Fluid and Plasma Dynamics Conference, Palo Alto (CA), USA, 1981.

[30] R. Collercandy. *Multigrid Strategy for Euler and Navier-Stokes Computations for Flows around Complex Aerospace Configurations.* In ECCOMAS CFD Conference, Athens, Greece, 1998.

[31] A. Lerat, J. Sidès and V. Daru. *An Implicit Finite-Volume Method for Solving the Euler Equations.* Lecture Notes in Physics, Vol.17, Springer-Verlag Ed, 1982.

[32] J. Cahen, V. Couaillier, J. Délery and T. Pot. *Validation of Code using Turbulence Model Applied to Three-Dimensional Transonic Channel.* AIAA J., Vol.33, No.4, 1995.

[33] N. Liamis and V. Couaillier. *Unsteady Euler and Navier-Stokes Flow Simulations with an Implicit Runge-Kutta Method.* ECCOMAS CFD Conference, Stuggart, Germany, Wiley-Interscience-Europe Ed., 1994.

[34] N. Liamis. *Méthodes Implicites de Résolution des Equations d'Euler pour des Ecoulements Tridimensionnels Instationnaires dans des Turbomachines.* PhD thesis, ENSAM, 1993.

[35] C. Benoit. Personal communication.

[36] J. Reisz. *Analyse Expérimentale d'une interaction choc-couche limite turbulente à Mach 1.45.* ONERA RT No.44/7078 AY, 1981.

[37] A.L. Gaitonde. *A Dual-Time Method for the Solution of the Unsteady Euler Equations.* Aeronautical Journal, October, 1994.

[38] N.D. Melson and M.D. Sanetrik. *Multigrid Acceleration of Time-Accurate Navier-Stokes Calculations.* 7th Copper Mountain Conference on Multigrid Methods, Copper Mountain (CO), USA, 1995.

[39] Y. Huang, P. Cinnella and A. Lerat. *A Third-Order Accurate Centred Scheme for Turbulent Compressible Flows Calculations in Aerodynamics.* Proceedings of ICFD, Oxford, England, 1998.

[40] P. Cinnella, Y. Huang, V. Couaillier and A. Lerat. *Accurate Simulation of Turbulent Transonic Flows over Oscillating Airfoils.* ECCOMAS CFD Conference, Athens, Greece, 1998.

[41] C. Benoit. *Auto-Adaptation de Maillages en Aérodynamique par Utilisation d'Algorithmes Génétiques.* 30ème Congrès National d'Analyse Numérique, Arles, France, 1998.
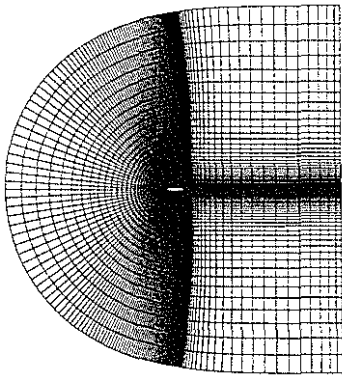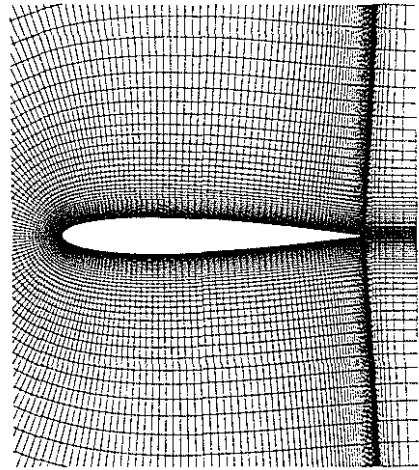
Figure 1: Global view of the airfoil
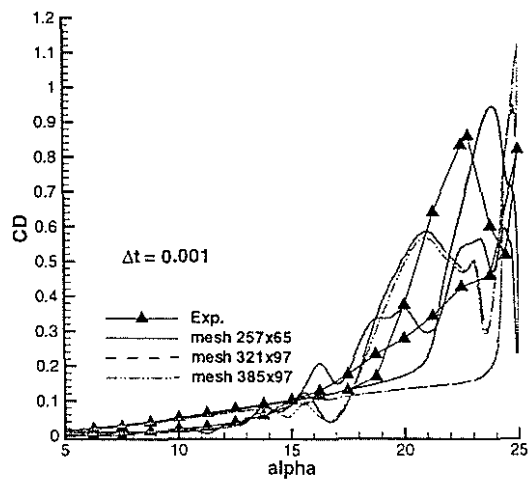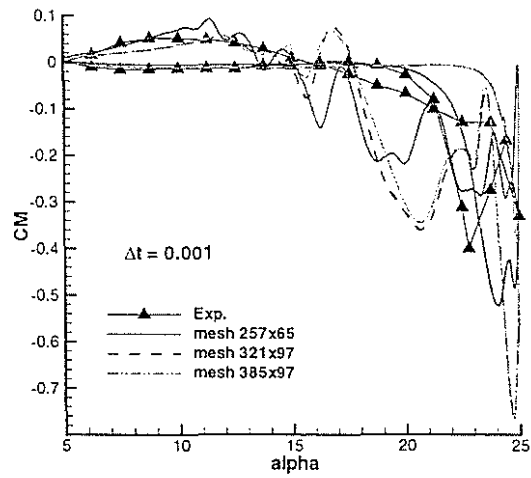

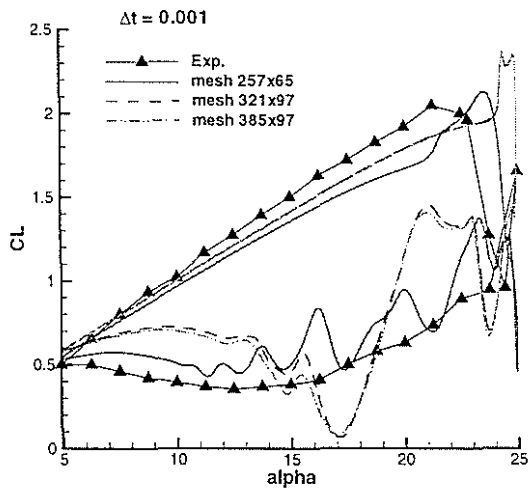Figure 2: Close view of the airfoil

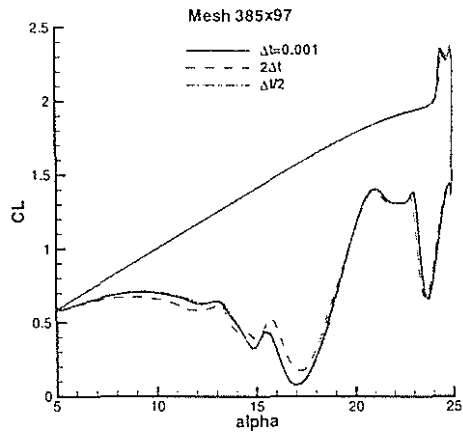Figure 3: Effect of the grid - $\Delta t = 0.001$

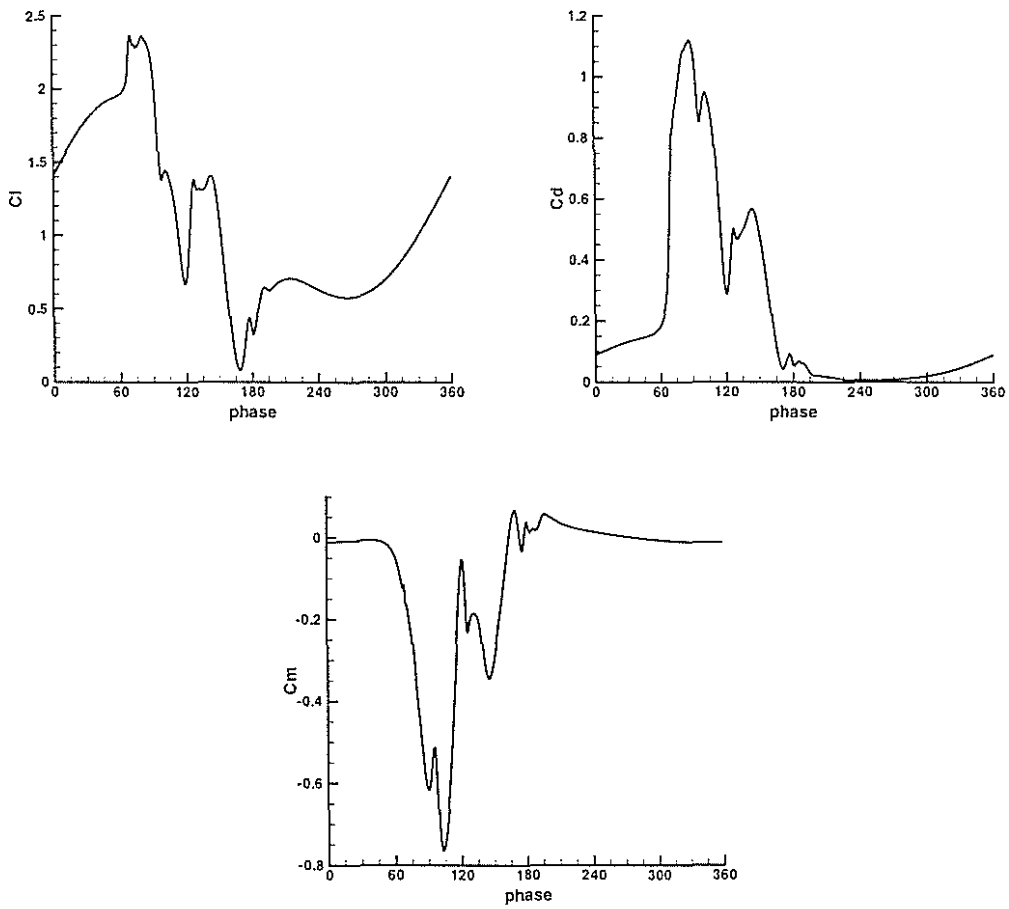Figure 4: Effect of the time step - Grid 385x97
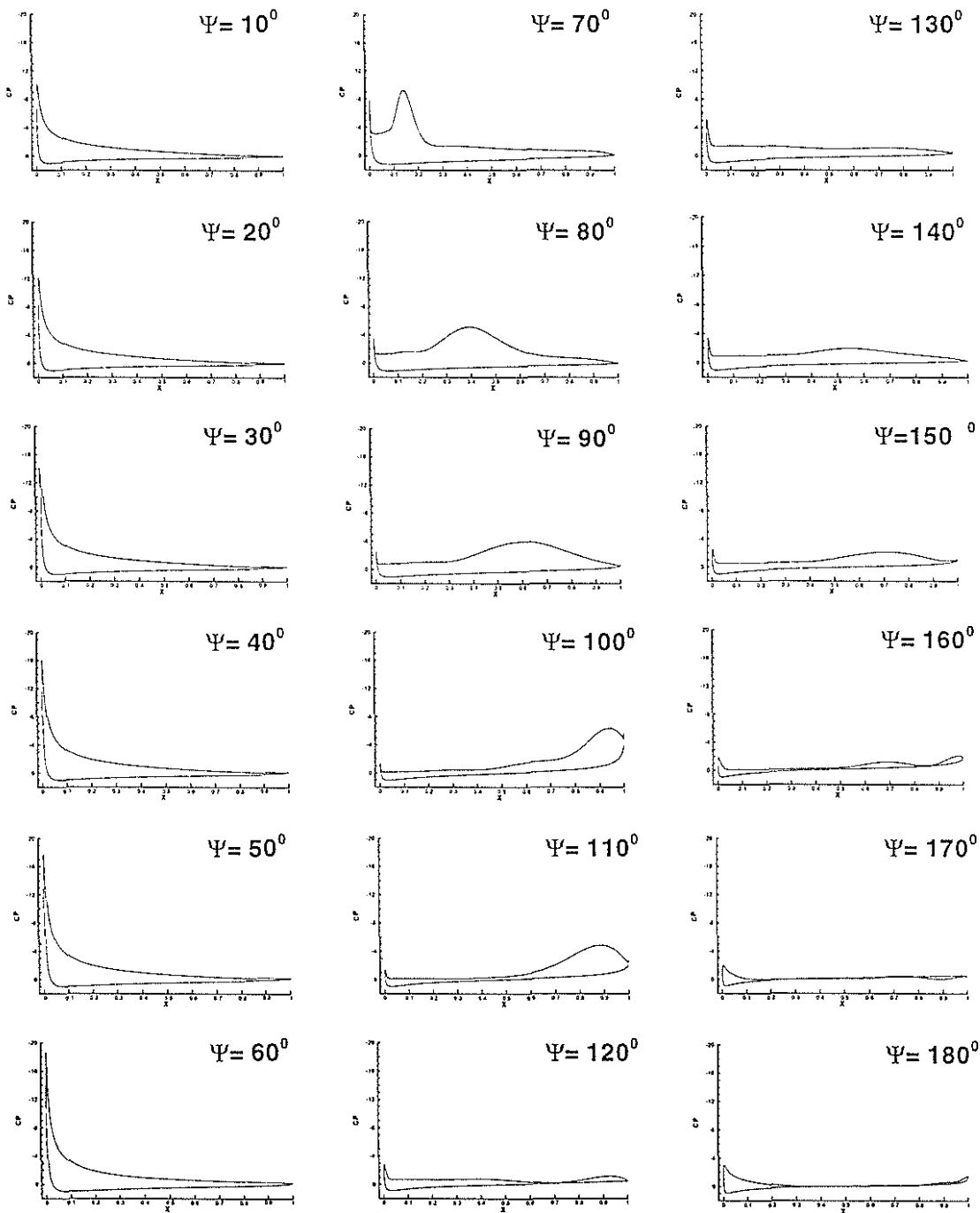

Figure 5: Lift, drag and moment coefficients

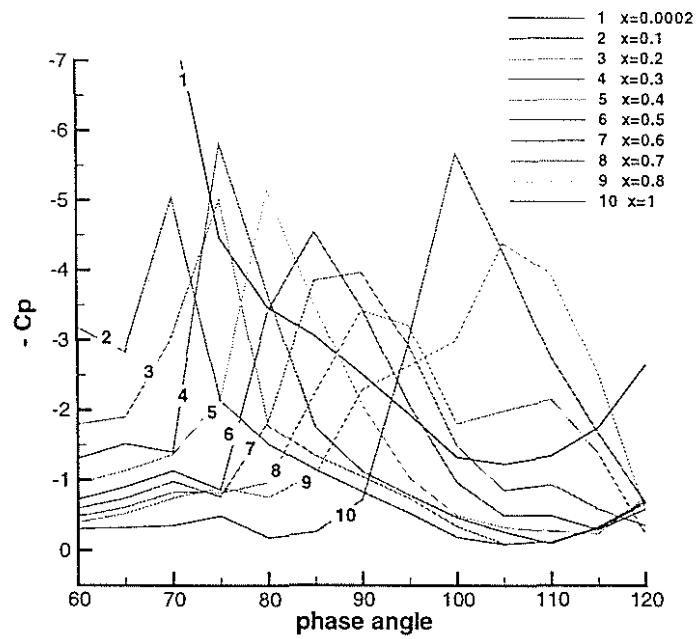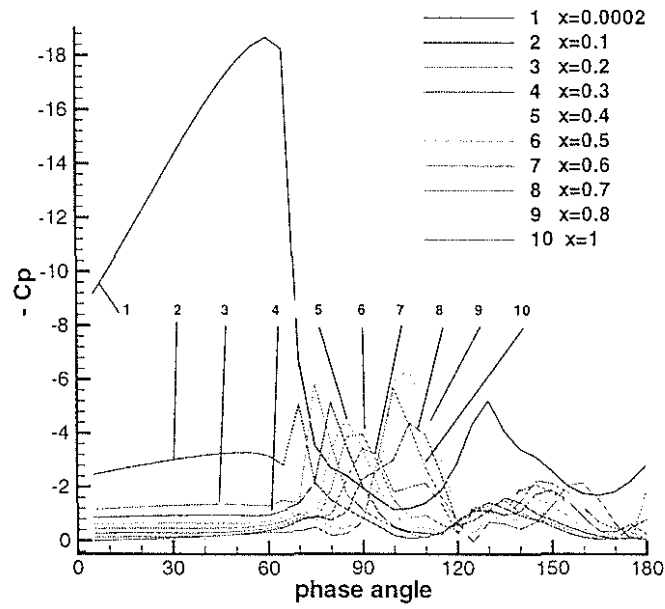Figure 6: Pressure distribution on the airfoil surface - Grid 385x97 - $\Delta t = 0.001$

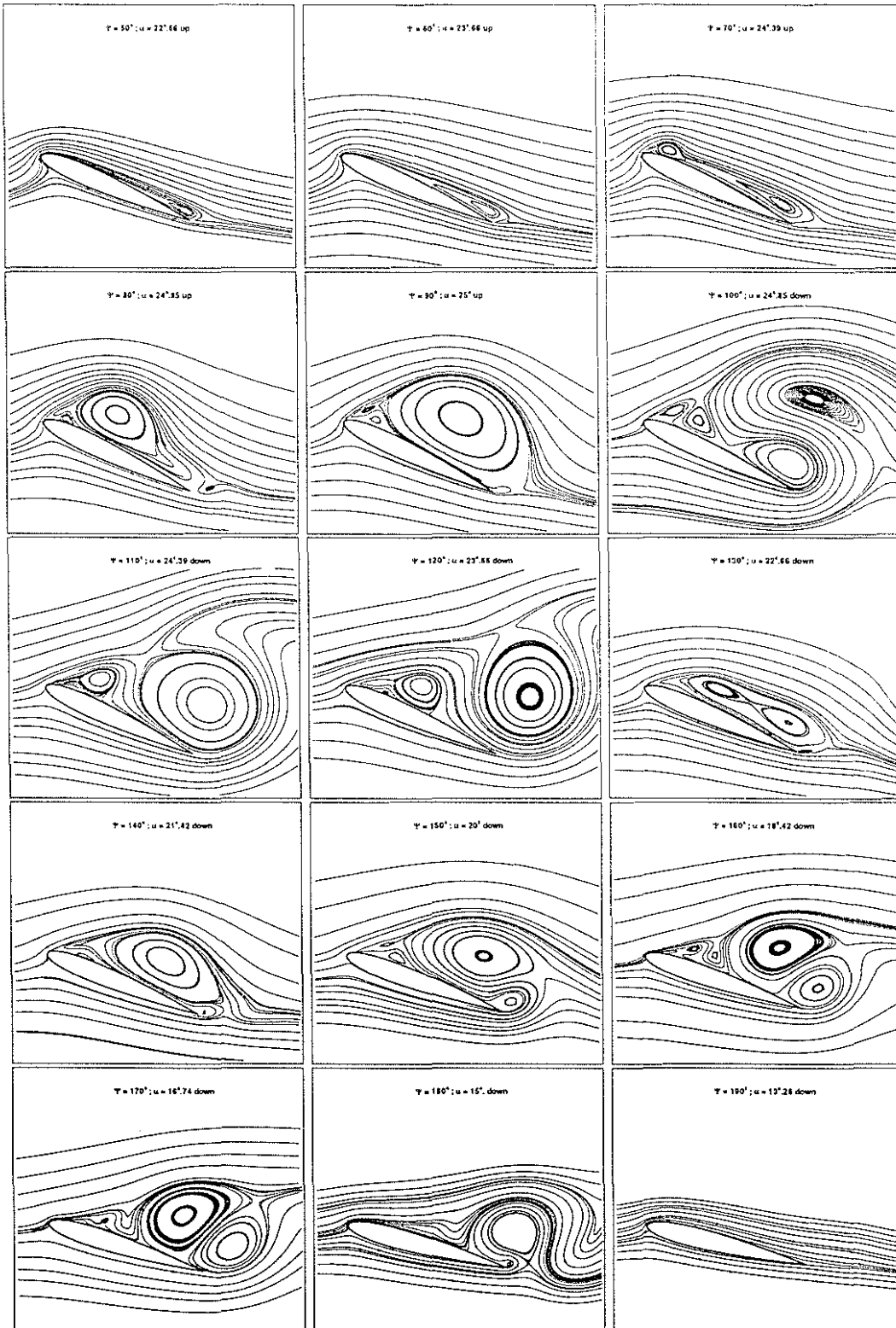Figure 7: Pressure on the airfoil surface vs phase angle - Grid 385x97 - $\Delta t = 0.001$

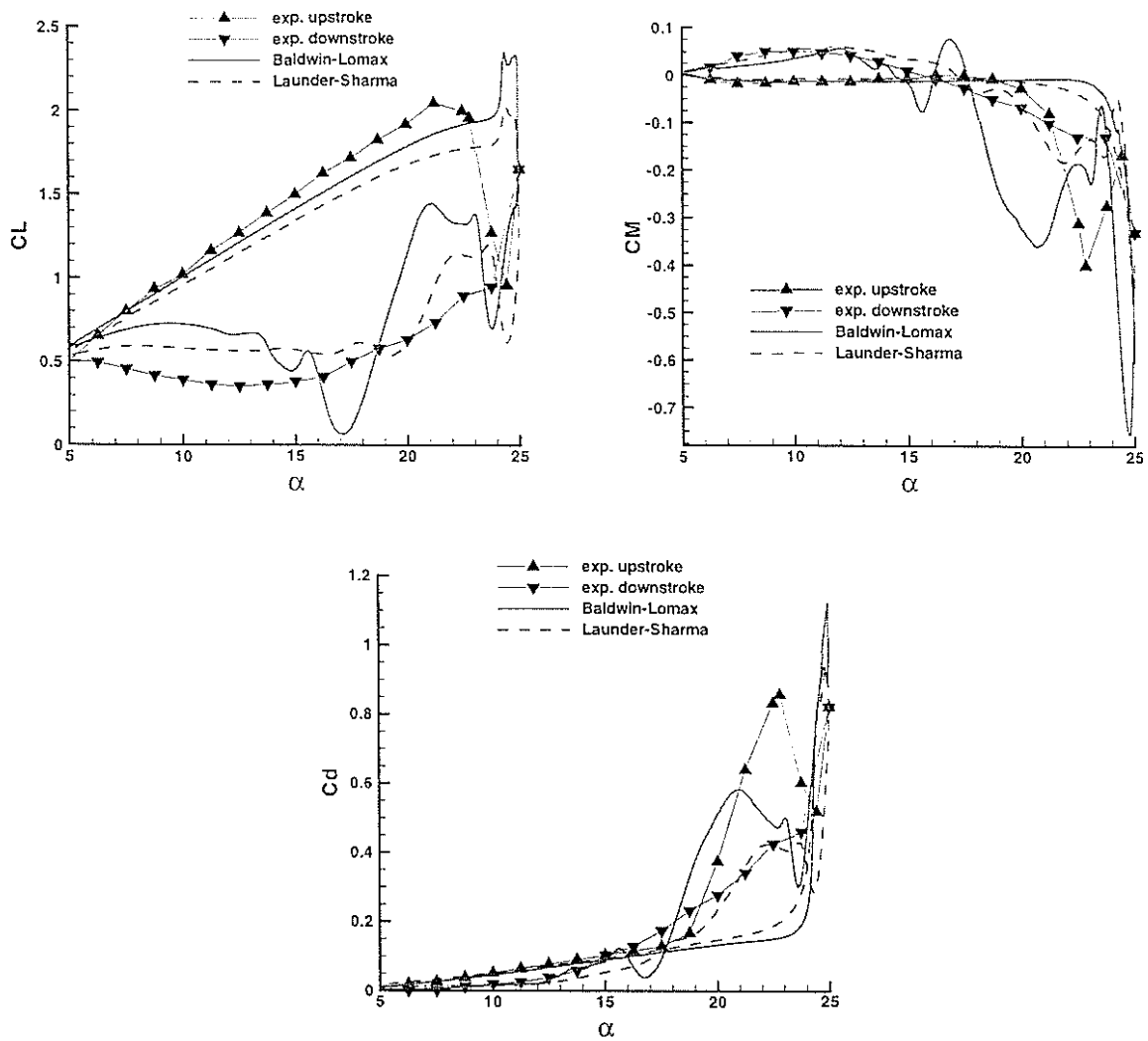Figure 8: Instantaneous streamlines - Grid 385x97 - $\Delta t = 0.001$

Figure 9: Comparison of the global coefficients
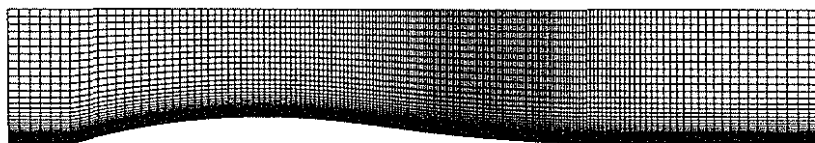
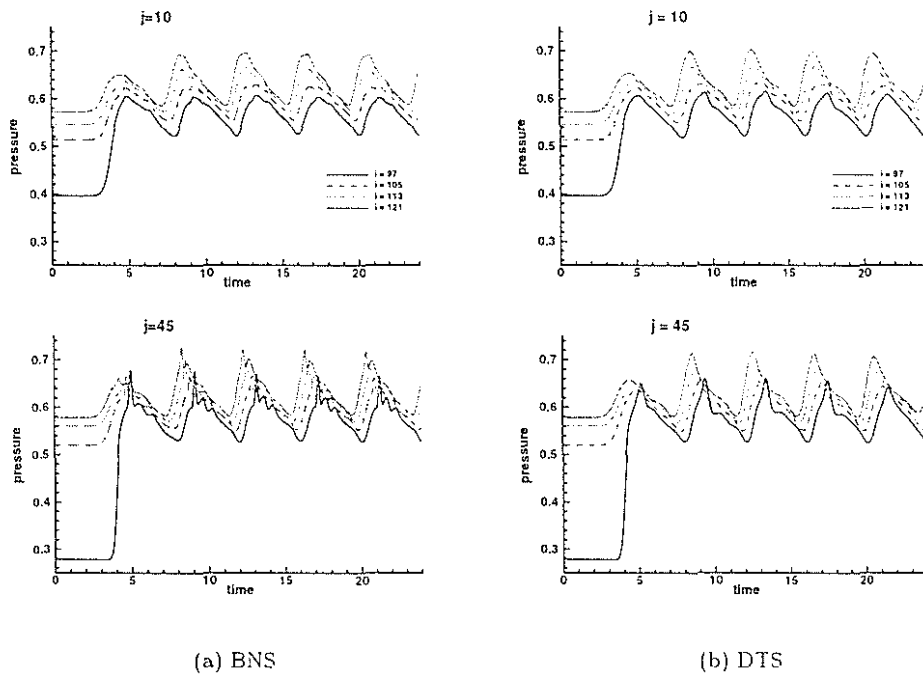Figure 10: Grid of the channel flow test case

(a) BNS

(b) DTS

Figure 11: Time evolution of the pressure - Channel flow - $\Delta t = 0.1$
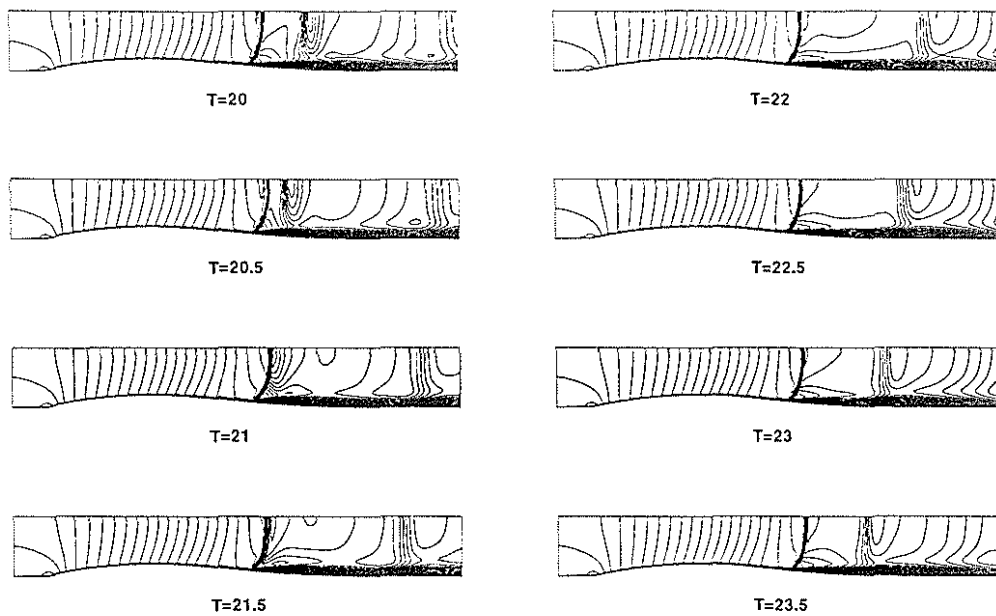

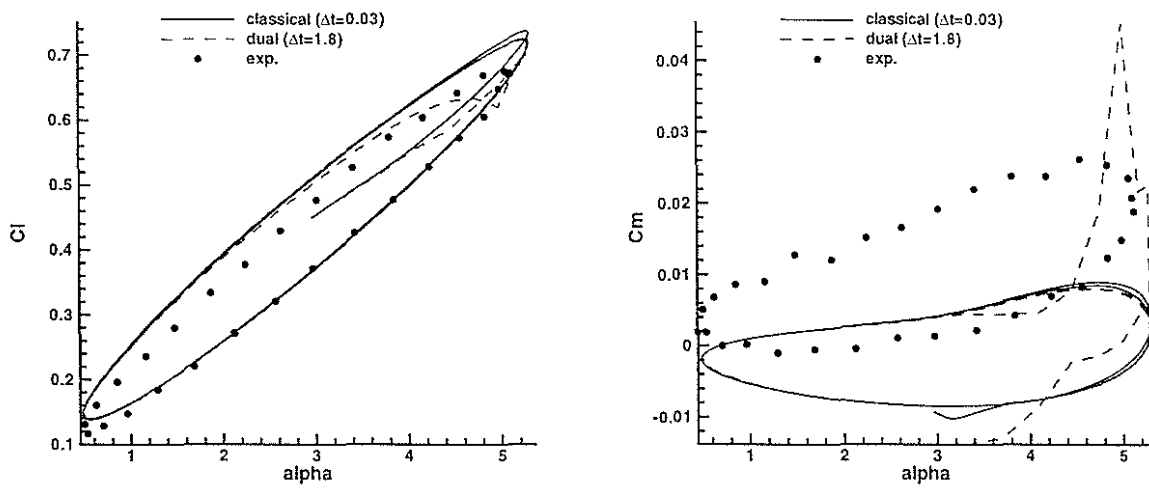Figure 12: Time evolution of the Mach number contours - Channel flow - $\Delta t = 0.1$

Figure 13: Lift and Moment coefficient - AGARD CT1 test case